An Analysis on the Astronomical Neighbourhood and the Observable Universe

PHYS3080 Distance Ladder Report

Ryan White
s4499039

with collaborators Ciaran Komarakul-Greene & Leo Clarke

April 14, Semester 1 2022

Abstract

The results obtained in this report build upon previous astronomical surveys to incorporate groundbreaking data obtained by the Pimbblet Picture Producer satellite, and the associated conclusions. Using all-sky surveys in several wavelength bands over the course of one year, a distance ladder was constructed of the observable universe with objects of minimum brightness 10^{-17} W.m^{-2}.nm^{-1}. In the local universe, stars were found to be clustered in coherent galactic structures, with many galaxies belonging to spheroidal clusters in the distant universe. Using three key distance relations, properties of local and distant galaxies were inferred with relationships obtained between galaxy luminosity and mass, mass and maximum rotational velocity, amongst others. Most notably, precise colour-magnitude diagrams and rotation curves were formulated for all nearby galaxies with resolved stars, and the distant galaxies were found to be unanimously approaching our local universe with a well defined distance-velocity trend. Qualitative and quantitative results and inferences were discussed with associated implications to the fundamental physical properties of the universe.

1 Introduction

The recently launched and retrieved Pimbblet Picture Producer space probe (PPP) has provided a great opportunity to study our universe in a way never been done before. In recent years, a concerted effort of New Earth's scientific and engineering communities resulted in a series of probe launches that studied the local universe. In the data that followed, mostly general qualitative results were obtained. Perhaps the most relevant of the conclusions from previous studies (specifically for this report) were on the nature of stars our galaxy; the stars emit radiation following a blackbody curve with element absorption lines. The general form of such a luminosity curve is given by

$$L(\lambda, T) = \frac{8\pi^2 hc^2}{\lambda^2} \frac{a}{\exp\left(\frac{hc}{\lambda kT}\right) - 1} \tag{1}$$

where h, c and k correspond to Planck's constant, the speed of light, and Boltzmann's constant respectively, while a is a constant depending on the telescope, star, and distance properties. Equation (1) directly correlates higher temperature blackbodies with a lower wavelength peak in the emission spectrum; hotter objects will appear more blue in the visible spectrum of light.

In the published literature to date, stars, at least in the local neighbourhood, have been found to almost entirely belong to large clusters arranged in a disk-like orientation. This is because, as a large cloud of gas condenses, conservation of angular momentum necessitates that the velocity increases proportionally to the radius decrease. Due to frictional forces between parcels of gas, the motion of gas will become increasingly coherent over large timescales which results in (observed) smooth velocity profiles. As these gas parcels condense further, star formation is initiated with the stars following the trajectories of the progenitor gas parcels. During this report, these collections of stars may be referred to as star clusters or galaxies interchangeably.

With the launch of the PPP and a year of high-resolution data taking, previous results can be enhanced with quantitative analyses. Over the course of one year in orbit around New Earth, the PPP took observational data on all three Cartesian axes in the sky resulting in six, long exposure images (a picture for each positive and negative axis). In each of these images, objects brighter than 10^{-17} W.m^{-2}.nm^{-1} could be resolved, with their luminosities in three wavelengths recorded. Using spectrographic data from onboard instruments, the doppler shift of the objects could be quantified by

the shift in element absorption lines, and hence the radial velocity of objects determined. On top of these images, the PPP could infer parallax angles of close objects from a narrow-field camera which observed light-sources at 6-month intervals. As the most comprehensive all-sky survey done yet, the PPP also carried with it an X-ray monitor which was extremely sensitive to short duration pulses of light. The data that these instruments collected provided a rich framework on which to analyse the physical properties of the Universe.

2   Methods and Results

Throughout the entire project, the programming language Python was used for automatic analysis of the large data set. With this, a number of packages were utilised for integral calculations to the results, namely: SciPy, NumPy, Astropy, and Matplotlib, with the package Pandas used for ease of data access.

As a first objective of the project, the data from each of the 6 images needed to be combined into a unified coordinate frame on which the remaining analysis could be performed. The format in which the data was supplied consisted of x and y coordinates, $x, y \in [-45°, 45°]$, for each star, with the center of each image at $(x_0, y_0) = (0°, 0°)$ for each of the six image orientations: "front", "right", "back", "left", "up" and "down". Naturally, this was not friendly to automated analysis across the whole sky, and so each of the equatorial-centered images ("front", "right", "back" and "left") were stitched together accordingly. The "up" and "down" images were subject to a rectangular-to-spherical coordinate transform upon being stitched in the appropriate places to the equatorial-centered images. To account for the stitching of locally defined coordinates (per image), all coordinates were transformed to a unified spherical coordinate system defined by three parameters: $r \in [0, \infty)$ — the distance away from the origin, $\phi \in [0, \pi]$ — the polar angle (with $\phi = 0$ at the geographic north pole), and $\theta \in [0, 2\pi)$ — the equatorial angle (with $\theta = 0$ at the center of the "front" image).

Given this unified coordinate system, maps of both the observed point-like objects and fuzzy objects were produced in (an approximated form of) true colour with the size of the object corresponding to its apparent luminosity. These maps are shown in Figures 1 and 2 respectively.
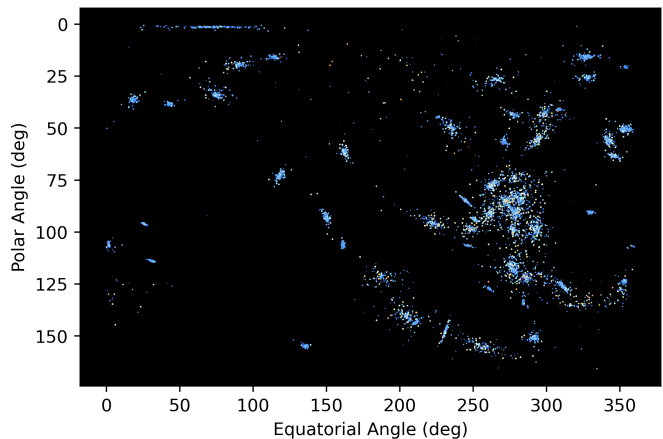

Figure. 1   Map of Observed Stars
This map shows some isolated structure in the universe as seen from New Earth, with some clustering of stars visible. This figure exaggerates the colour of the stars as a by-product of the colour-sampling method, and does not represent what would be seen by the eye. The scale of the stars in the image are based on a logarithmic normalization of all the stars, with dimmer stars appearing smaller.
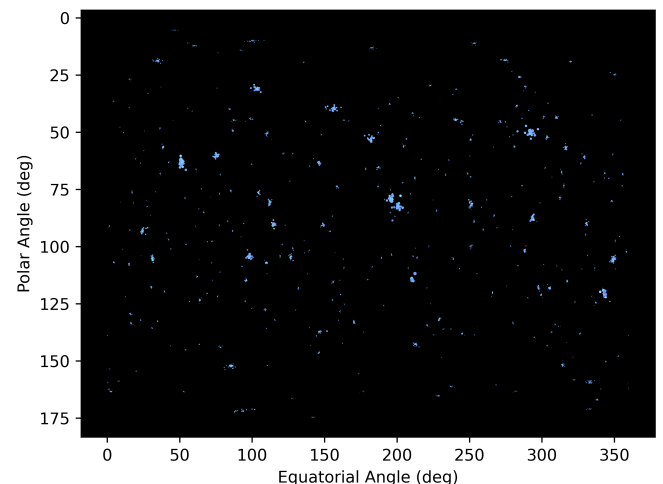

Figure. 2   Map of Observed Fuzzy Objects (Galaxies)
As in Figure 1, the size of the objects in this image are not indicative of real size but apparent brightness, with larger sizes corresponding to brighter objects.

Worth noting in each of these figures is the apparent warping at the polar extrema. This is due to the spherical sky being mapped with respect to a rectangular projection, and so the apparent area density of objects is not preserved.

2.1   Temperature Profiles

To understand more complex relationships between observables in the sky, first the nature of the objects which are being observed must be understood. In the

local universe, galaxies are resolved into clusters of stars, and so defining the characteristics of these stars is paramount. As the emission spectra of stars are known to adhere to a blackbody spectrum depicted in equation (1), finding the temperature of the stars allows for the inference and explanation of other observations (as will be elaborated on further in the report).

Since the spectroscopic data provided by the PPP is in the form of blue, green and red fluxes (wavelengths of 440nm, 500nm and 700nm respectively), finding the temperature of a star is done by fitting a blackbody curve to it's spectra. Using the aforementioned SciPy package (specifically the `curve_fit` function), the data could automatically be fit to a blackbody curve with a dimensionless constant (relating to the distance and intrinsic luminosity of each star) and the temperature as the output. Over all resolved stars, the histogram of temperatures found are shown in Figure 3. The spectral energy distributions of six example model fits are also shown in Appendix 5.2, with all of the fits available in the linked GitHub repository. The blackbody model was deemed an excellent fit to the observational data on inspection of all of the produced fits.
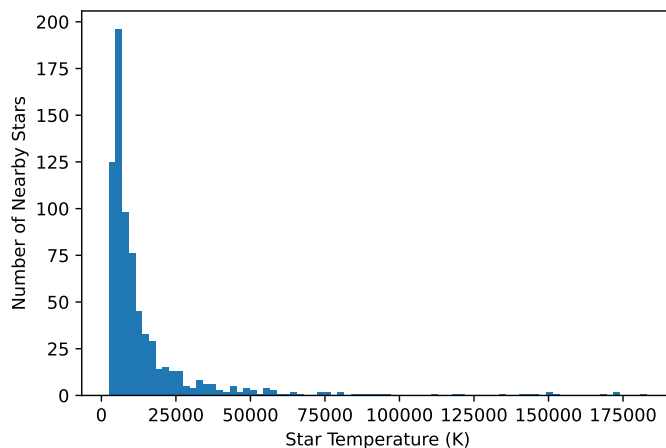

Figure. 3 Complete Distribution of Stellar Temperatures

Sample size consists of all of the resolved stars brighter than 10^{-17} W.m^{-2}.nm^{-1} in the sky. Minimum star temperatures were on the order of 3000K, while maximum observed were about 190000K. The domain was split into 50 bins of equal width. The magnitude of uncertainty in the temperatures were proportional to the fit temperature, with $\sigma_T \approx 300$K for stars of about 4000K, and an order of magnitude higher for stars of temperature 10^5K.

This distribution of stellar temperatures is very clearly skewed towards the right (higher temperature). The reason for this is discussed in the discussion section of this report. Taking a more concentrated view of the main-sequence star temperatures (3000K $\leq T \leq 50000$K), results in the distribution shown in Figure 4.
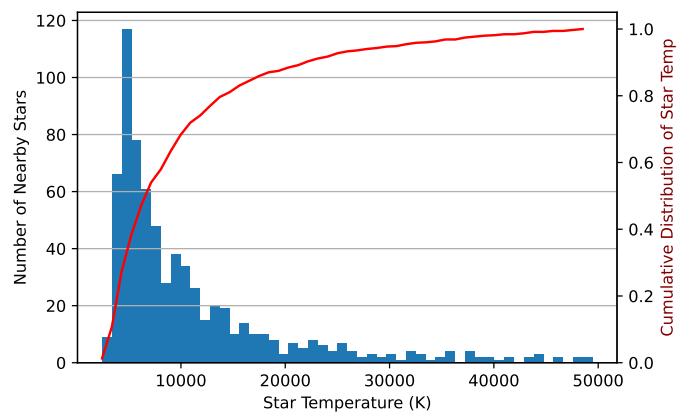

Figure. 4 Main Sequence Stellar Temperature Range Distribution

This is a magnified version of Figure 3 in the range of typical main-sequence stars. As with that figure, the domain was split into 50 bins of equal width. The cumulative distribution curve overlay shows an approximately logarithmic relationship between stellar count and increasing temperature, indicating that the vast majority of stars have temperatures less than 10000 ± 400K.

With the nature of stars in the local universe more firmly understood, relationships and bias between other observables can more easily be inferred as will be discussed further on.

2.2 Star Clusters and Nearby Galaxies

As Figures 1 and 2 clearly show, both stars and galaxies alike tend to belong to a coherent structure in the form of a disk-shaped and spheroidal clusters respectively, at least optically. In order to infer the properties of these clusters, their members must be collectively partitioned, with the method of doing so varying on whether the clusters are composed of stars or galaxies.

2.2.1 Star Cluster Identification from Redshift Profiles

To discern coherent structure of star clusters, the radial velocity of each star in the sky was plotted against the corresponding coordinates. What resulted is shown in Figure 5:
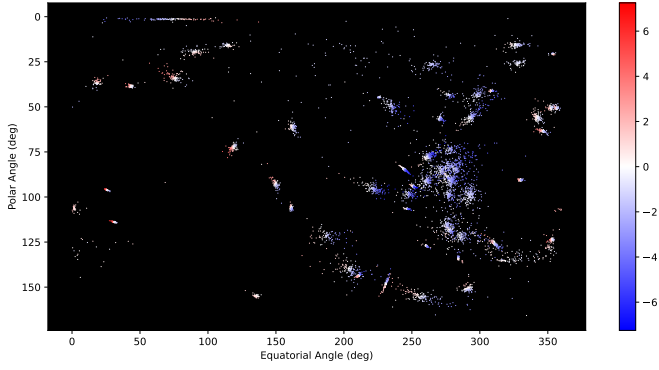
Figure. 5 Redshift Map of Observed Stars

This figure shows an all-sky map of resolved stars, with the colour of the stars corresponding to their respective radial velocity; blue points represent stars moving towards the observer, and red points represent stars moving away.

Each cluster of star in Figure 5 is characterised by a gradient of radial velocity from one side to the other. With this in mind, ellipses were manually fit to each of the 52 identified star clusters and the parameters of each ellipse stored for use later on in the analysis. Examples of this are shown in Figures 6a and 6b.
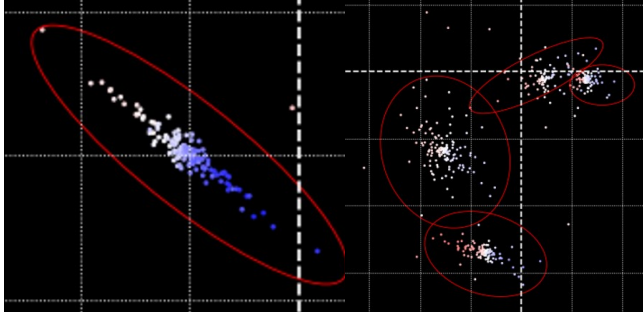
(a) Galaxy X245-Y85-N141 A perfect edge-on galaxy.

(b) An Optical Cluster of Galaxies

Figure. 6 Two Examples of Manual Galaxy Identification

Each galaxy is characterised by a smooth radial velocity gradient across its diameter, and the red ellipse surrounding it defines its angular bounds. The two images were taken from different sections of the sky, and the scale in the figure is not consistent.

The complete picture of identified nearby galaxies (with accurate angular scale) is shown in Appendix 5.5.

It is worth noting that star clusters were identified strictly on the basis of two criteria: that they displayed a smooth doppler gradient across their diameter, and that they were sufficiently (optically) isolated from other star clusters. The former criteria is a physical one, as actual (rotating) structures should display this feature, or at least some degree of it. The latter criteria is based on ease of analysis in that optically isolated clusters carry with them less interference from neighbouring clusters

(in the form of noise in the data set).

For the purposes of the report and classification, galaxies are named according to their central $\theta = x$ and $\phi = y$ coordinates, and the population of constituent stars. For example, the galaxy X245-Y85-N141 is has its center at $(\theta, \phi) = (245°, 85°)$, and is comprised of 141 resolved stars.

2.2.2   Galaxy Cluster Identification

The task of identifying clusters of galaxies within the sky required a fundamentally different approach compared to that of identifying clusters of stars. As Figure 7 shows, there are far too many optical clusters to perform manual operations of identification and so a fully automated method was required.
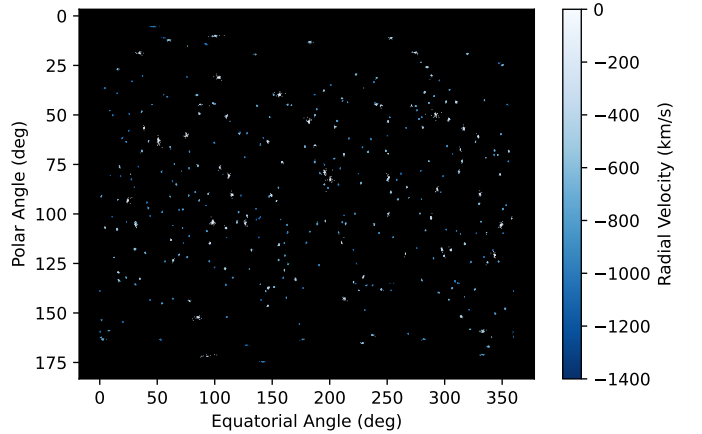

Figure. 7 All-Sky Redshift Galaxy Map

As with Figure 5, objects are coloured according to their radial velocity, with a deeper blue corresponding to a larger velocity towards the observer.

Perhaps the most interesting feature of Figure 7 is that galaxy clusters are composed of galaxies with near identical blueshift. Furthermore, galaxies with a higher blueshift tend to be grouped in a tighter angular distribution (i.e., have a smaller angular extent in the sky). As such, an algorithm for determining the angular extent for which a galaxy cluster could be considered bounded was devised and is given as

$$\Delta\theta = \Delta\phi = 2 + 10\exp\left(\frac{-|v_r|}{500}\right) \qquad (2)$$

which gives a maximum-allowed angular diameter of a cluster of approximately 8.7 degrees for clusters at blueshift of 200km.s^{-1}, and approx. 2.7 degrees for clusters at a blueshift of 1300km.s^{-1}, each of which are considered relatively low and high blueshifts respectively.

Similarly to galaxies, galaxy clusters were named according to their central position, population size and their radial velocity. For example, the cluster "AC-X23-Y132-N31" is an approaching cluster, centrally located

at $(\theta, \phi) = (23°, 132°)$, with 31 galactic members. Some distinction was made between 'clusters' of galaxies and 'groups' of galaxies, with the former corresponding (arbitrarily) to population sizes of $N \geq 20$, and the latter corresponding to populations of $3 \leq N < 20$.

2.3   Distance Estimation

Since the inverse square law of light has such an effect on how we view the universe, inferring the distance to luminous objects is the logical first step in estimating their intrinsic brightness. There are a few ways to estimate the distance to a light source, with the each applicable method discussed in this subsection.

2.3.1   Parallax Measurements

Due to the high resolution parallax mapping from the narrow-field camera onboard the PPP, parallax angle measurements were available for nearby stars. With these angle measurements, p, provided in units of arcseconds, the distance to such stars were calculated simply by

$$d = \frac{1}{p"} \text{ parsec} \qquad (3)$$

Since the minimum possible parallax measurement was $p = (1 \pm 1 \times 10^{-3})$ arcsec, all analysis done using parallax distance estimates were only carried out if the parallax angle was greater than 0.007 arcsec to maximise the signal-to-noise ratio above 85% and still maintain a reasonably large dataset. With this cutoff threshold, the maximum distance inferred from parallax was approximately $d = 143 \pm 21$ parsec, with proportionally lower uncertainties for closer objects.

2.3.2   Variable Star Period-Luminosity Relationship

Given that two classes of variable stars were observed at distinct luminosity ranges in Figure 12, the next step was to determine if there is a coherent relationship between the period and the luminosity of a variable star. The data provided from the PPP for each variable star was in the form of a flux-vs-time graph, with the the variability graph of the star P00179 shown as an example in Figure 8.

The variability period of each star was determined through a python implementation of the Lomb-Scargle periodogram, where the data was fit to trigonometric function via a least squares fit and the period of the curve output as the stars' variability period. In cases where the signal-to-noise ratio was unacceptable, the data was ignored and that star removed from the variable dataset. With all of the valid variable stars' (of known distance
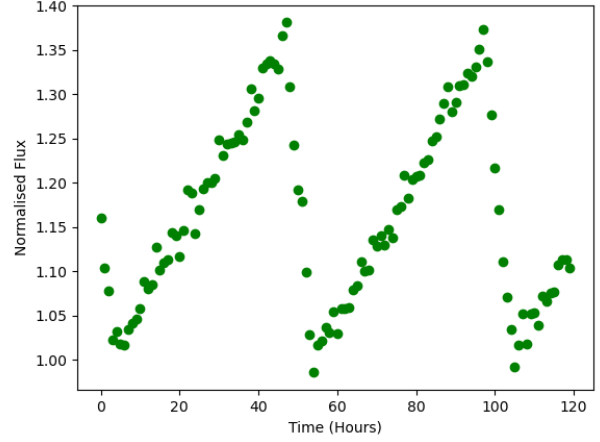

Figure. 8   Flux over Time for the Star P00179
The x-axis is in units of hours since first observation, and was measured over the course of 5 days. The y-axis is in the dimensionless units of normalized flux, as a multiple of some baseline flux determined on a star-by-star basis.

from parallax estimation) periodicity determined, the absolute magnitude of each star could be plotted against its period.
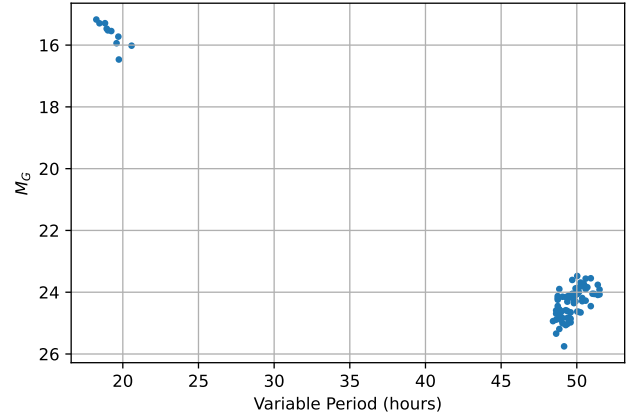

Figure. 9   Absolute Magnitude of Variable Stars vs their Periodicity
Clearly, two distinct classes of variable stars emerge when plotted with their 500nm absolute magnitude against period. The class 1 variables cluster around $M_G \approx 15$ and $P \approx 18$ hours, while the class 2 variables cluster around $M_G \approx 24$ and $P \approx 50$ hours.

Evidently, there are two distinct classes of variable stars, each with roughly linear relationships between magnitude and periodicity. First looking at the short period (class 1) variables, the relationship between magnitude and period is shown in Figure 10.
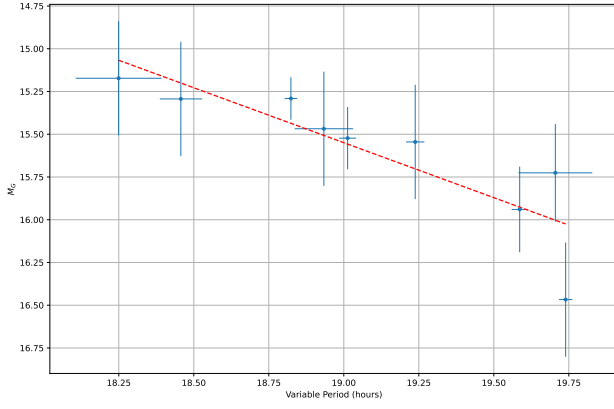
Figure. 10 Absolute Magnitude vs Period for Class 1 Stars

Uncertainties in period were found by a Monte Carlo simulation, and uncertainties in magnitude were due to both distance and flux uncertainty propagation.

Where the linear relationship is shown by

$$d_{\text{short}}(P) = \sqrt{\frac{\exp(-P/(1.56\,h) - 3.3)}{F_G}} \pm \sigma_d \text{ pc} \quad (4)$$

where the σ_d value is the propagated uncertainty in the measurement and depends on the parameters of the star, and $h = 1$ hours^{-1}. The equation to calculate this is given further in the report in equation (6).
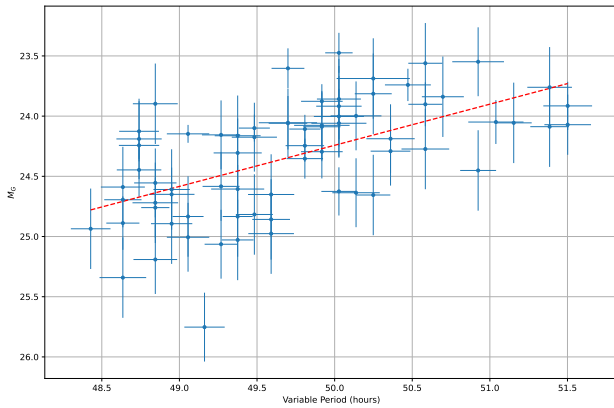Similarly for the longer period, class 2 stars,

Figure. 11 Absolute Magnitude vs Period for Class 2 Stars

Uncertainties were found by the same methods as in Figure 10.

And once again, the equation of best fit is given by

$$d_{\text{long}}(P) = \sqrt{\frac{\exp(P/(2.94\,h) - 41.3)}{F_G}} \pm \sigma_d \text{ pc} \quad (5)$$

The uncertainty in measurement (for both equations (4) and (5)) is given by

$$\sigma_d = \frac{d}{2}\sqrt{(\sigma_m P)^2 + \sigma_c^2} \text{ pc} \quad (6)$$

where $(\sigma_m, \sigma_c) = (0.05, 0.9)$ for short period variables and $(0.01, 0.5)$ for long period variables. The equations within this subsection together make up a more or less complete method of determining distance to a star given its variability. Due to the far smaller sample size of class 1 stars compared to class 2 stars (the Discussion elaborates on why this may be the case), the trend defined for long-period stars is generally more accurate and should preferentially be used. Class 1 stars, however, have the advantage of being orders of magnitude brighter than their long period counterparts and so are important indicators of distances at scales where class 2 stars are too faint to be resolved in current-generation telescopes.

2.3.3 Colour-Magnitude Diagrams

The next step of the distance ladder project involved finding the distances to objects too far to show a parallax measurement. By plotting all of the stars from an isolated star cluster onto a colour-magnitude diagram, a vertical shift of the cluster's data curve to align it with a benchmark curve indicates the approximate distance to said cluster. Of course, one must have a benchmark curve to begin with.

After the distances to nearby stars were found, their intrinsic luminosity was found when accounting for the degradation in light intensity as a function of distance. With distance known, the *absolute magnitude* of a star can be calculated from the specific flux (of band i) by:

$$M_i = -\ln(F_i) - 2\ln(d) \quad (7)$$

When the absolute magnitude in each wavelength was found, all of the nearby stars were plotted on a colour-magnitude diagram shown in Figure 12.

Note that the colour values obtained for a cluster of unknown distance is always accurate, since, from equation (7),

$$M_B - M_R = -\ln(F_B) - 2\ln(d) - (-\ln(F_R) - 2\ln(d))$$

$$= -\ln(F_B) + \ln(F_R) = \ln\left(\frac{F_R}{F_B}\right)$$

and so observed colour is independent of distance.
The aforementioned vertical shift in M_G (the absolute magnitude of flux at 500nm), ΔM_G can be used to infer distance. By rearranging equation (7), one obtains

$$d = \sqrt{\frac{\exp\left(-\Delta M_G\right)}{F_G}} \text{ pc} \quad (8)$$

For entire clusters, determining the shift was a trivial, but manual, process. Since the galaxy X245-Y85-N141 is a textbook example of an edge-on galaxy, many of the visualisations in this report display this galaxy's data. The *shifted* colour-magnitude diagram for this galaxy is shown in Figure 13
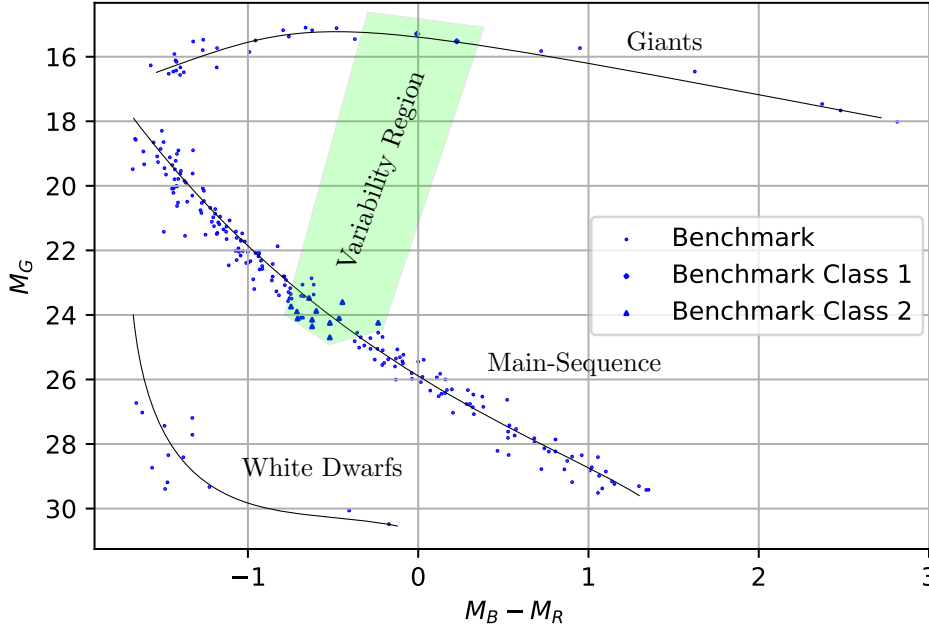
Figure. 12 Annotated Colour-Magnitude Diagram of Nearby Stars

Each star may be classified by its position on the C-M Diagram; Main Sequence stars are characterised by relatively long lifespans and hydrogen burning, White Dwarf stars are the final stage in a stars life, and Giant stars represent the bright final years of a star characterised by helium shell burning.

There is a distinct Variability Region in which stars will pulsate with some periodicity. Class 1 stars are giants with low periodicity ($P < 25$ hrs), and Class 2 stars are main-sequence with high periodicity ($P > 25$ hrs).
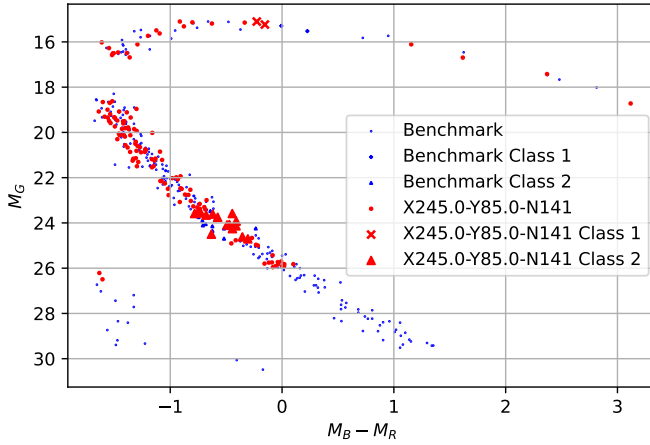

Figure. 13 Colour-Magnitude Diagram for X245-Y85-N141

All of the stars within the diagram have been shifted by an amount corresponding to $d \approx 693 \pm 50$ pc. Note the identical colour-magnitude trend between the two data sets. The uncertainty in corresponding distance was a result of the maximum shift difference between arbitrarily defined upper or lower distance bounds of fit, and the benchmark data set.

Of course, this process was carried out for each nearby galaxy for which stars could be resolved (and hence a colour-magnitude diagram produced), and the corresponding distances calculated. As is discussed further on in the report, galaxy radii (at least the calculated angular radii on the basis of the maximum angular distances subtended by member stars of a galaxy) are typically on the order of several tens to two hundred parsec in absolute radius. Given that most nearby galaxies are on the order of several hundred to a few thousands of parsec in distance, the distance error for each star within a constituent galaxy is reasonably low when its distance is taken as the galaxy's distance.

2.3.4   Distance Estimation Methods in Conjunction

Both the colour-magnitude vertical shift method and the period-luminosity relations rely on initial parallax distance calculations for calibration, but having two separate methods raise the question of how well they agree. Due to the aforementioned poor sample size that formed the basis of the short-period luminosity relation, distance measurements conducted by equation (4) were often far out of agreement with the colour-magnitude and long period distance estimations. The measurements taken by both the colour-magnitude and long period estimations were almost always in agreement within uncertainty, with a standard deviation of their differences of approximately 100pc for clusters of distance on the order of 10^3 pc.

2.3.5   X-Ray Source Analysis — Distance of Far Galaxies

Throughout the whole year of PPP observations, 52 distinct X-ray flashes were observed originating from various galaxies at random positions in the sky. This results in a frequency (per galaxy) of

$$\text{Frequency} = \frac{52 \text{ X-Ray Flashes per year}}{11287 \text{ Galaxies}}$$
$$\approx 4.6 \times 10^{-3} \text{ yr}^{-1}$$

And so, on average, we would expect a flash about once every 220 years from a particular galaxy, assuming that all galaxies experience roughly the same frequency of X-ray flashes (there is no property of a galaxy that makes

it more likely to produce a flash).

Perhaps the most interesting aspect of these X-ray flashes is that they all have approximately the same intrinsic luminosity, since they all have the same exact wavelength after accounting for blueshift effects. This means that they may be used as a tool to infer distance over scales where stars cannot be resolved (and consequently where the other distance methods aren't applicable).
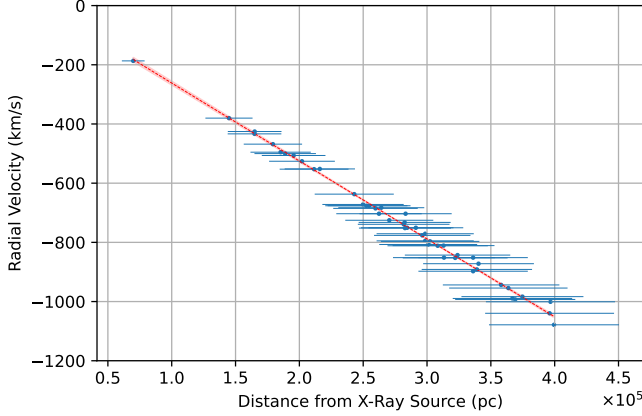

Figure. 14 Cluster Velocity vs Distance from Associated X-Ray Source

The linear fit to the data associated extremely well, with $R^2 = 0.994$. The uncertainty in photons received by each X-ray flash (and hence the brightness and distance estimates) was $\sigma = 16.7$, with the receiver being sensitive to counts of 282 photons or more.

The associated trend with the data in Figure 14 is

$$v_r = (-263 \pm 3) \times 10^{-5}\, d + (1.64 \pm 8.98)\ \text{km.s}^{-1} \quad (9)$$

Which gives a value for the Hubble constant of

$$H_0 = (-2.63 \pm 0.03) \times 10^3\ \text{km.s}^{-1}.\text{Mpc} \quad (10)$$

The implications of this will be discussed in the Discussion section of the report. In the mean time, this result provides an accurate method of determining distance to those galaxies too far to resolve stars; a direct calculation of distance from their observed radial velocity.

2.4   Galaxy Analysis

With distance known to a reasonable uncertainty of all observable galaxies, now other observables can be accurately associated with galactic parameters.

2.4.1   Rotation Curves

Since galaxies display a smooth doppler gradient across their diameter, with extremal values furthest from the central region, a plot of the rotational velocity of each star as a function of distance from the center should yield a smooth curve. Indeed, taking the median equatorial and polar angles of the stars within a galaxy as the geographic center, and plotting the velocity of each star

produces such a curve as seen in Figure 15.

However, each galaxy as a singular structure carries with it an average radial velocity with respect to the observer. This radial velocity, taken as the midpoint between the maximum and minimum observed velocities, was subtracted from all of the radial velocities of the galaxy's constituent stars to obtain a distribution with a mean velocity of approximately zero. Also, the angular distance between the center and the most distant star within the galaxy, ϑ, was taken as the (angular) galactic radius. Although not relevant to a plot of rotational velocity vs radius (where radius is a proportion of galactic radius), this allows the calculation of the absolute galactic radius, R_G, via

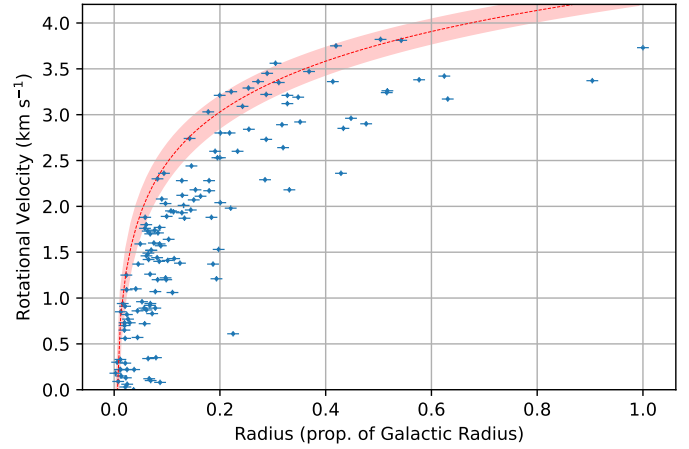$$R_G = d \cdot \tan \vartheta \quad (11)$$

Figure. 15   Rotation Curve of Galaxy X245-Y85-N141

A logarithmic trendline was plotted to the velocity ceiling of the data via the NumPy `polyfit` function with $\ln(r)$ as the x input. Uncertainties were calculated via the square-root of the diagonalized covariance matrix that was output from the `polyfit` instance.

The actual rotation curve needed to be fit on the "ceiling" of the velocity-distance data points as this is where the true maximum rotational velocities at some radius r from the center were displayed. This was done computationally by first sorting all of the velocity-radius data in order of increasing radius, and checking if the next data point (with higher radius) had a higher rotational velocity than the current one. All of the data points for which this "increasing-radius to increasing-velocity" relationship held were added to an array, where the rotation curve was fit to data in that array. The majority of fits had an $R^2 > 0.95$, with some as high as $R^2 = 0.991$ and the lowest being $R^2 = 0.509$. In each curve with $R^2 < 0.9$, anomalous data points were found, likely as a result of some stars not actually belonging to the galaxy in question, but being optically aligned. A more advanced method of star cluster (galaxy) identification would reduce the number of falsely assigned stars to a galaxy.

Notice that in Figure 6, both edge-on and inclined galaxies display unusually low stellar radial velocities

in the axis perpendicular (but still within the disk) of the maximum *observed* velocities. This is a result of those stars having a larger ratio of tangential/proper motion to radial motion, and so while all of the stars at radius r are moving at nearly constant velocity, they are doing so with different direction which results in a lower observed radial velocity. Those stars with higher tangential velocity appear to sag underneath the curve (trendline, or data ceiling) in Figure 15.

There remains one final aspect of galaxy rotation curve derivation that has not been explained: correction for galaxy inclination relative to the observer. Face-on galaxies would of course be characterised by comparatively low radial velocity observations compared to that of an analogous edge-on galaxy due to the aforementioned misaligned velocity vectors. To account for this, the ellipticity of the ellipses which defined each galaxy were calculated and compared to that of the perfectly edge-on galaxy X245-Y85-N141. This example galaxy was thereafter assumed to have true radial velocity measurements, and any galaxy which had a lower ellipticity (relative to the observer) had their component stars' radial velocities multiplied by some factor dependent on the inverse cosine of the ellipticity; galaxies that were more edge-on had a smaller multiplicative factor, while more face-on galaxies had a larger one to account for the inclination.

While only one representative rotation curve was shown above, a rotation curve for each nearby galaxy was calculated and plotted (available on the GitHub repository). Each curve followed the same logarithmic shape, and a stacked (and normalized) plot of all of the curve shapes is shown in Figure 16.
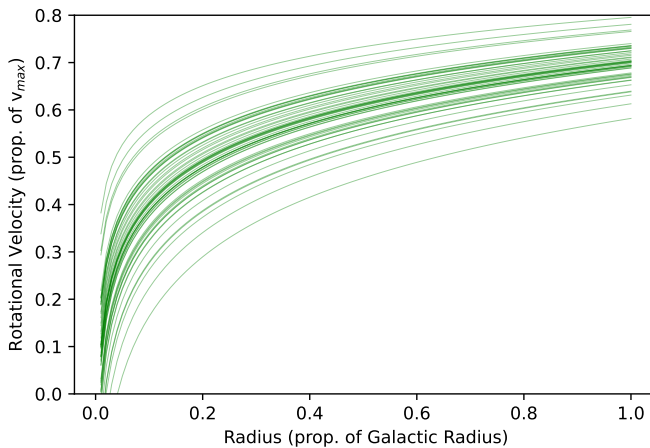

Figure. 16 Stacked and Normalized Galaxy Rotation Curves
Each curve was plotted with an alpha of 0.4, so darker regions in the plot correspond to a more common velocity profile. All curves were normalized against the maximum rotational velocity of all galaxies.

The implications of the shape and consistency of these graphs will be explained in the Discussion section.

2.4.2 Properties of Nearby Galaxies

Since the distance to nearby galaxies and their respective rotation curves is known, estimation of their other properties is viable. By the Virial Theorem, an estimate of the mass of a galaxy can be obtained:

$$v_{\max}^2 = \frac{GM}{R_G} \Rightarrow M = \frac{R_G v_{\max}^2}{G} \tag{12}$$

Using this formula inputting the previously defined galactic properties allows for the calculation of mass of all nearby galaxies. Plotting the mass against maximum rotational velocity within the galactic disk results in Figure 17.
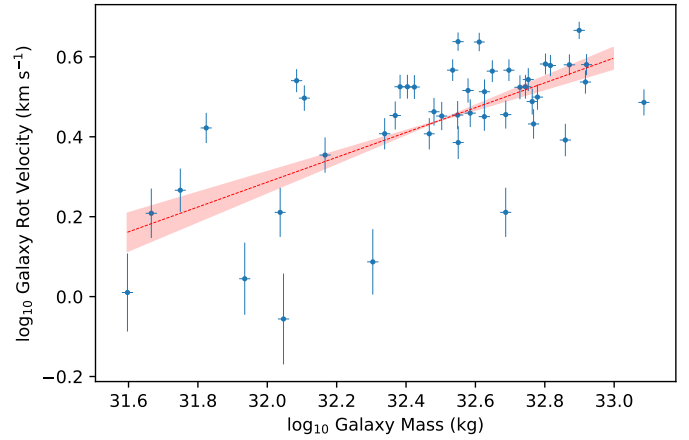

Figure. 17 Galaxy $v_{\max}$ vs Mass
A reasonably well defined linear model fits the data, with $R^2 = 0.438$. Due to the uncertainty propagation laws, values of higher $\log_{10}(v)$ yield more certain results. The uncertainty in mass was found via a Monte Carlo simulation, with varying galactic radius and $v_{\max}$. Due to computational expense, only 50 Monte Carlo simulations were calculated per data point.

The linear trend in Figure 17 is given by

$$v_{\max} = e^{(-9.66 \pm 1.72)} M^{(0.31 \pm 0.05)} \text{ km.s}^{-1} \tag{13}$$

with uncertainties in the trend parameters given by the square-root of the diagonalized covariance matrix produced by the `polyfit` function, as before.

Unfortunately, galactic mass and maximum rotational velocities are not observables for distant galaxies and so to infer the behaviour of galaxies in the far universe, a relationship between an observable and another parameter must be formulated. Given that the distance to distant galaxies can be estimated by the Hubble law relation, the luminosity of galaxies serves as a suitable observable. Plotting the galactic mass of nearby galaxies with respect to their luminosity (centered at 500nm — the V band) gives Figure 18.
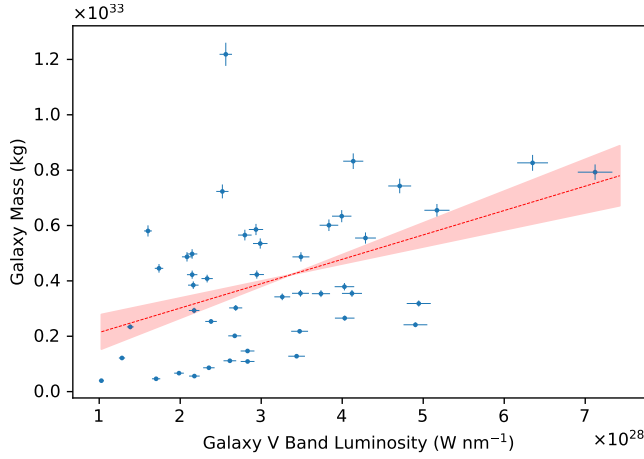
Figure. 18 Galactic Virial Mass vs Green Luminosity
The linear model fit to some degree, with $R^2 = 0.198$. Three anomalous data points were ignored due to several order of magnitude disparities against the remainder of the data, both in virial mass and in luminosity.

The linear model fitting the data is described by

$$M = (8.81 \pm 2.67) \times 10^3 \, L_V + (1.25 \pm 0.09) \times 10^{33} \text{ kg} \quad (14)$$

where the specific luminosity (in units of W.nm^{-1}) was calculated from flux measurements and the distance by

$$L_V = 4\pi d^2 F_V \quad (15)$$

Another key observable is the size of a galaxy, which, when combined with known distance, allows for the inference of actual galactic radius. Plotting the galactic radii of nearby galaxies against their virial mass gives Figure 19.
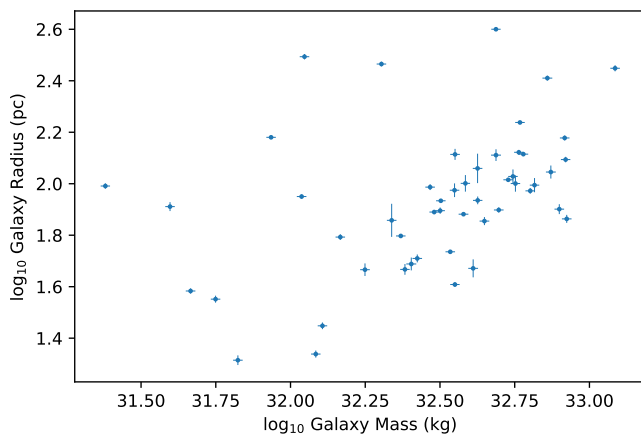

Figure. 19 Galactic Radius vs Virial Mass
Due to the sparse distribution of data points, no fit was attempted. Uncertainties in radius were propagated from formulae used, and were notably proportional to the distance to the galaxy. Hence, larger errorbars in $\log_{10}(R_G)$ represent galaxies at a larger distance.

Further studies are recommended to refine this data and produce a model that fits the data, for which there seems to be some correlation especially at higher mass.

2.4.3 Galaxies Afar

Now that the distance to distant galaxies can be inferred from the Hubble law, the validity of the cosmological principle can be discussed. By observing the spatial number density of galaxies across equal-volume concentric spherical shells, the principle of homogeneity could be somewhat quantified. The resulting relationship between distance and galaxy number density is shown in Figure 21.
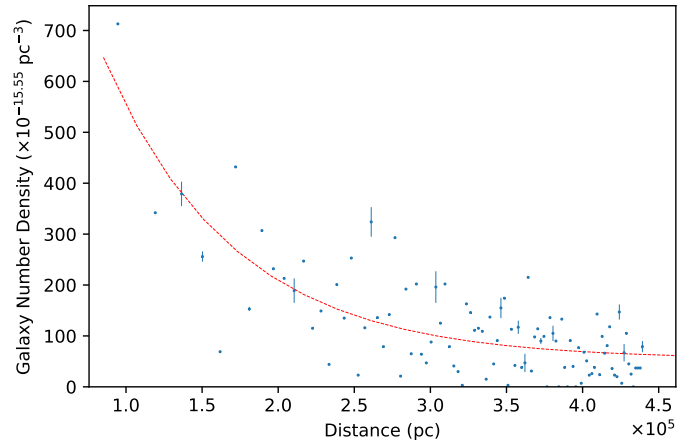

Figure. 21 Galaxy Spatial Number Density vs Distance
The volume of each of the 100 concentric shells, with inner bounds of radius 0pc, and upper bound of approx 4.59×10^5 pc — representing the border of the observable universe — resulted in approximately $V \approx 10^{15.55}$ pc^3. Uncertainties in number density were calculated based on the uncertainty in galaxy distance, and so if a galaxy could feasibly belong to two concentric shells within uncertainty, the magnitude of the uncertainty for that particular shell was increased by 1. The model fit follows that of an inverse exponential law, but in analysis it was found that a power law could comfortably be fit to the data with a similar R^2 value.

The inverse exponential law relation between the spatial galaxy number density against distance can at least in part be explained from observational bias. Since the cameras on the PPP had a minimum brightness threshold for which objects could be detected, any object dimmer than 10^{-17} W.m^{-2}.nm^{-1} would not be accounted for in the dataset. As such, the cameras preferentially detected disproportionately bright and/or close galaxies.

The second aspect of the cosmological principle is on the matter of isotropy. An isotropic universe is one that has no large-scale preferential structuring to a matter distribution, and so the distribution of matter
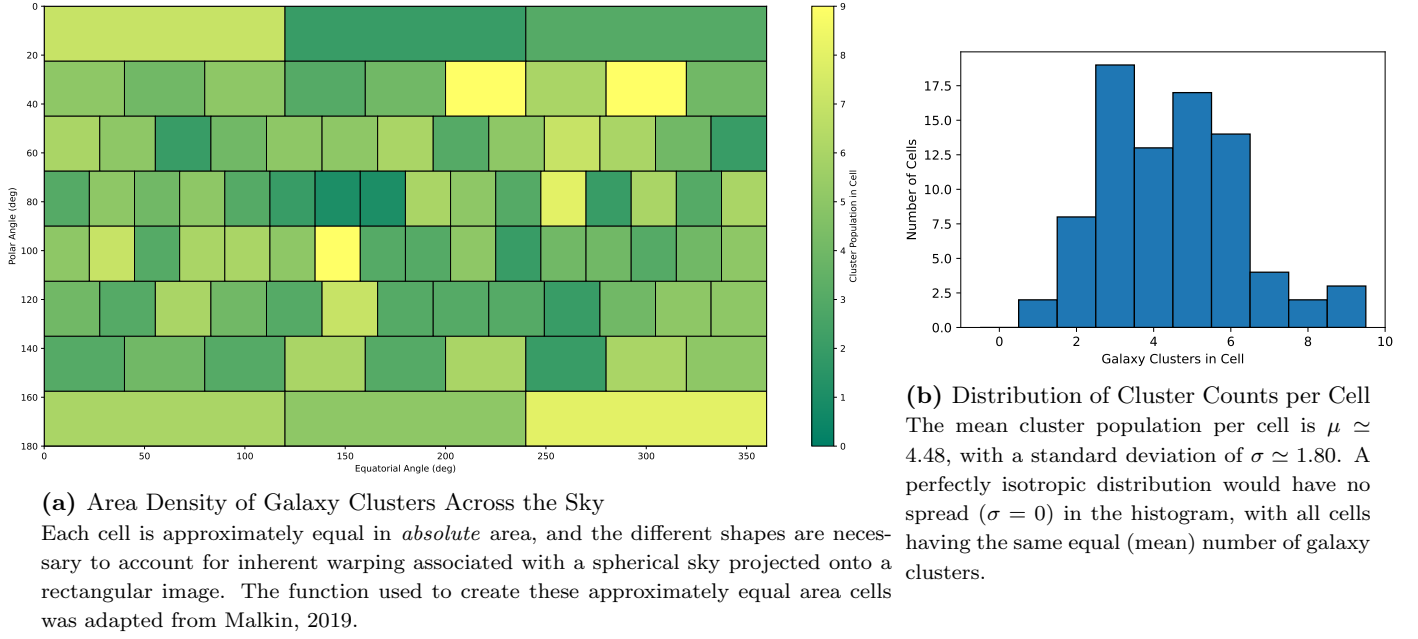
(a) Area Density of Galaxy Clusters Across the Sky
Each cell is approximately equal in *absolute* area, and the different shapes are necessary to account for inherent warping associated with a spherical sky projected onto a rectangular image. The function used to create these approximately equal area cells was adapted from Malkin, 2019.

(b) Distribution of Cluster Counts per Cell
The mean cluster population per cell is $\mu \simeq$ 4.48, with a standard deviation of $\sigma \simeq 1.80$. A perfectly isotropic distribution would have no spread ($\sigma = 0$) in the histogram, with all cells having the same equal (mean) number of galaxy clusters.

Figure. 20   All-Sky Area Density of Galaxy Clusters, with Histogram of Distribution

should appear more-or-less random over a sufficiently large angular scale. Figure 20a shows the galaxy cluster spatial area distribution across the sky. Across all cells, there appears to be no significant structure of galaxy clusters. Figure 20b supports this by showing that the cluster cell count per equal-area cell follows an approximate uniform distribution of mean 4.48 and standard deviation 1.80. Since the standard deviation is relatively low compared to the mean, most cells have a roughly equal number of galaxy clusters within their bounds with no significant optical under/overdensities. The implications of this will be further discussed in the next section.

By the same process of equation (13), the virial mass of a galaxy cluster can be estimated from the velocity dispersion of the constituent galaxies within. Since the galaxy clusters were defined earlier, finding the velocity dispersion and radius of each cluster was a simple task. The cluster radius was taken to be half of the angular extent between the two most separate galaxies within the cluster, where the absolute radius was found by equation (11). The velocity dispersion of the galaxy was found by taking the the absolute difference between the maximum and minimum radial velocities, and multiplying by three to account for each axis of rotation (assuming that galaxy clusters unanimously cluster into spheroidal distributions with randomly aligned velocity vectors for each constituent galaxy).
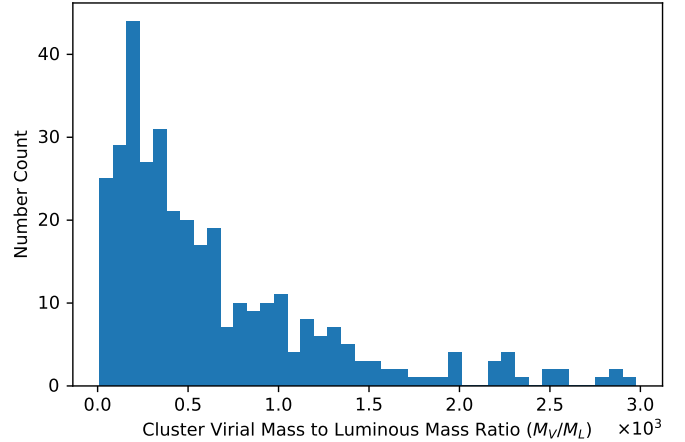

Figure. 22   Galaxy Cluster Virial to Luminous Mass Ratio Distribution
The mean of the distribution was found to be $\mu \simeq 637$, with a standard deviation $\sigma \simeq 597$. The histogram is defined by 40 bins of equal width.

Figure 22 shows that any particular galaxy cluster's virial mass is consistently larger than its' respective luminous mass (found by the summation of the mass of each constituent galaxy, where the luminous mass was calculated from V-band luminosity as per equation (14)).

3   Discussion

With all of the data collected and analysed, the task is now to infer why the universe is structured in the way we observe. Starting from the local universe and expanding our view outwards, each result will be qualitatively

explained with reference to related physical phenomena and quantitative results given in the previous section.

3.1 The Local Neighbourhood

We begin with very local neighbourhood of nearby stars. In the Results section, two notable relationships between stellar parameters were observed: the distribution of stellar temperatures as a function of the number of stars, and the relationship between the colour of a star and it's luminosity. These two observed phenomena are intrinsically linked, as the colour-magnitude diagrams x-axis represents a stars colour which is fundamentally determined by its temperature via the distribution of the Planck curve (eq. (1).

Both Figures 4 and 12 agree that the vast majority of observed stars are redder in colour, with Fig. 4 specifically indicating that the majority of these redder stars lie on the main-sequence where the spend the majority of their lives. A main-sequence turning point (where main-sequence stars transition to the giant branch) far within the blue colour suggests that the stars in the universe are quite young, as some of the more massive stars (and hence hotter and bluer) still lie on the main-sequence.

Figure 12 shows the region in which stars display a variable flux curve, with two distinct groups observed. As was alluded to before, there was a significantly smaller sample size of class 1 (low period) stars which is due to their position on the colour-magnitude diagram which indicates they belong to the giant group of stars. If stars remained in their branch for equal amounts of time, we might expect that there would be approximately equal sample sizes of class 1 and 2 stars, but since there is such a deficiency in class 1 population, we expect that stars progress through the giant stage of evolution much faster than other stages.

An observation of note is that there appears to be a roughly constant distribution of main-sequence stars across the colour axis. Similar to the observational bias suggested with respect to the galaxy spatial number density (Fig. 21), we expect that this smooth distribution does not accurately represent nature. The proposed hypothesis is that there are *far* more low mass, red, and dim stars than those characterised by a higher temperature but that the PPP detectors could not resolve them over distance. What results is only the closest dim red stars seen, with an equal number of hot blue stars visible at great distance even though they may be rarer.

The proposed picture of stellar evolution follows: stars are formed from condensing gas clouds which, when sufficiently dense, produce an emission spectrum according to its temperature and chemical makeup (with absorption lines from select elements). The most massive, blue stars quickly progressed onto the giant phase on Figure 12 where they progressively cool and contract (perhaps due to mass loss via stellar wind which lessens the pressure on the core) until such a point where they shed their envelope and remain hot, dense objects with orders of magnitude lower luminosity than their former selves.

An interesting observation to note is that all local galaxies (with resolved stars) displayed the same turn-off points on their main sequence. This indicates that all stars, at least within the local universe, are the same age. On this note, given that there is only one turn-off point, we expect that there has only been one stellar formation round and that no new stars have been formed since the first round. This proposition doesn't necessarily hold if the second round of star formation made only low-to-intermediate mass stars which have not yet reached their turn-off age. For the sake of argument, however, we expect that any subsequent round of stellar formation could form stars as massive as the first round and so there would be higher mass stars of a younger age which would display another main-sequence turn-off point in conjunction with the singular observed one.

A key observation which supports the previous claim of observational bias in star population is that local galaxies, especially those at further distances, resolve far less low-mass, dim, and red stars (see Figure 13).

Aside from stellar properties, the scope of the discussion now turns to the closest galaxies including the one in which New Earth Resides. As Figure 23 (and the accompanying .gif file in the GitHub repository) show, New Earth is situated on the far edge of a disk galaxy. By some metrics, it could realistically be considered a field star (one that is isolated from any coherent galactic structure) but will be considered as part of the associated galaxy for the sake of this report. By analysis of this Figure, the distance of New Earth to the geographic center of the galaxy is $d = 50 \pm 5$ pc (calculated by a series of pythagorean expressions). See Appendix 5.4 for the associated diagram and estimated values.

Almost as one structure, Figure 23 shows two nearby spiral galaxies almost adjacent to our parent galaxy. Due to the proximity of these galaxies, their angular extent was too large to isolate their stars against a backdrop of more clearly defined galaxies and so they were not included in the analysis. This would be a crucial research topic for future studies of the local universe.
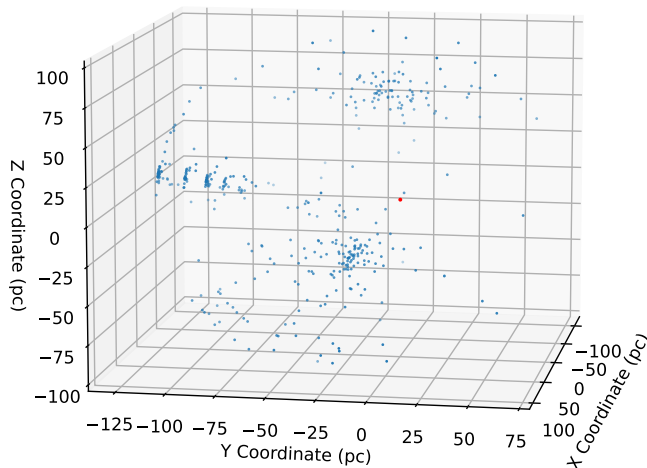
Figure. 23 The Local Neighbourhood Around New Earth

The red dot signifies $r = 0$; the position of New Earth. Clearly, New Earth resides at the outer edge of the lower-middle galaxy in the image. The concentric rings seen in the middle-left of the image are due to distance discontinuities as a result of low parallax angle (with the rings outside-in corresponding to parallaxes of $p = 0.008, 0.009, \ldots$). The distance uncertainties of ± 21 pc account for the apparent discontinuities (evident in the image) in all analysis. A rotate-able version of this figure is available in a Jupyter notebook in the projects GitHub repository; see Appendix 5.1. Also, please click this link for an animation of this figure rotating about the equatorial axis.

3.2   Local Galactic Cluster

As a direct result of locally resolved stars, New Earth's parent galaxy is part of a local galactic cluster with ≥ 52 apparent members (when accounting for local galaxies that could not be optically isolated from each other). The parameters of the majority of these galaxies were calculated in the results section, but a qualitative analysis is yet to be performed.

All of the local galaxies were found to be in a relatively flat disk shape due to the observed smooth doppler gradients across their diameters. For the galactic disks which have been observed edge-on (galaxy X245-Y85-N141 as an excellent example, shown in Figure 6a), there appears to be a spheroidal "bulge" of stars within their center. Generally, these bulges appear to have a height (component perpendicular to the disk) about 10-15% that of the disk radius. The disk itself, specifically at a radius of half of the disk radius, appears to have a height about 2-5% that of the disk radius. About half of the galaxies were observed to have only a sparsely populated bulge as opposed to the dense clustering seen in galaxy X245-Y85-N141. In most cases where a bulge was identified, an increased

spatial density of stars within the plane of the disk was observed too, indicating that there may be some distinct kinematic structure within the center of disk galaxies.

There was no observational evidence of significant galaxy interactions, where one might expect disk warping and/or high perpendicular (to the disk) velocity vectors for stars due to gravitational perturbations. Over a prolonged timescale, we would expect spheroidal distributions of stars (galaxies) as a result of galaxy mergers with misaligned angular momentum vectors. In this picture, two misaligned galactic disks would merge to form a spheroidal distribution with no coherent rotation curve after a "thermodynamic" cooling period of the constituent stars. Given that no galaxies with this distribution of stars was seen, we suggest that galaxies, and thereby clusters of galaxies, have not existed for long enough to display this stage of evolution.

The observed velocity profiles across each galactic disk have rich implications. By Newtonian gravity, as a particle moves further from the source of gravitation it's associated orbital velocity should decrease proportionally to an inverse square law. The velocity profile that follows from this is a peak in rotational velocity of stars in a galaxy part way from the center of that galaxy, which then gradually falls off as $r \to \infty$. This shape is expected from the centrally clustered stellar distribution within the galactic disk. This, however, is not what was observed from Figure 15. Instead, an approximately logarithmic velocity profile was observed in *all* nearby galaxies, where the rotational velocity consistently increased with increasing radius. This velocity profile suggests that there is some separate, and non-luminous mass distribution far from the center of galaxies which is accelerating objects deep within the potential well. Further studies could attempt to quantify this mass distribution, provided that the luminous mass of the galaxies were calculated as an expected baseline first.

The observed rotation curves also allow some other scientists' hypotheses to be tested. Opposing what some previous literature suggested, there appears to be *no supermassive black holes in the center of galaxies*. The proposed compact, non-luminous, and massive astronomical objects would necessitate a second (and sharp) peak of rotational velocity as $r \to 0$ within a galaxy due to the immense gravitational field in the local region of the galactic center. This sharp peak was not observed in any of the local galaxies. Further tests could investigate as to whether stellar or intermediate mass black holes lie within galactic centers, or perhaps a distribution of low-mass black holes in the galactic halos as an explanation for the non-luminous gravitational influence on the observed velocity profiles.

The relationship between the maximum rotational

velocity of stars within a galaxy and said galaxy's (luminous mass) follows from the aforementioned model of Newtonian gravity, where a larger gravitation potential as a result of clustered massive particles directly translates into a larger central acceleration and hence orbital velocity. This relationship was supported within the local cluster by Figure 17, where a reasonably well-fitting linear model described galaxies with larger mass having larger rotational velocity magnitudes.

What remains are the relationships between observables (over cosmological distance) and galaxy virial mass. Figure 19 shows a relatively coherent trend of increasing galactic radii with increasing mass, provided that the mass is sufficiently large to begin with. In practice, this is not necessarily a valid trend to infer due to the associated scatter in the plot for numerous galaxies that don't reach this mass threshold (of about $10^{32.3}$ kg). Mass aside, galaxies in the local cluster were found to be unanimously disk shaped with an average radius (in an approximate uniform distribution) of about 100 pc, with maximum radii found to be on the order of 180pc and a minimum at around 40 pc. Perhaps the more *consistent* (but not necessarily accurate) trend is that between galaxy V band luminosity and its associated mass. Although individual data points rarely fit accurately to the trend line, the systematic error is small and galaxies seem to coherently increase in mass with increasing luminosity.

3.3   The Far Universe

The physical relationships between observables in the distant universe were built upon the the relationship between radial velocity and distance as per the Hubble Law. The implications of equations (9) and (10), along with Figure 14 are profound, showing that the universe is contracting relative to our local region. Galaxies at larger distances are moving at an even faster rate. The cause of this contraction cannot be accurately determined from the data obtained in this report, and further studies are necessary to refine the data and better quantify the results. That said, the approximate time until these distant galaxies fully collapse into our local region can be given by the *Hubble time*: the inverse of the Hubble constant given in equation (10). Performing this calculation gives the estimated time until the "death" of the universe as 372 ± 5 million years. This assumes that the universe will continue to contract linearly with time, and that gravity will have no significant effect on the contraction rate once the galaxies fill a more compact volume (and hence interact more strongly via gravitation).

Given that all observed galaxies outside of the local cluster are observed with high blueshift, the apparent cause of contraction could be gravitational attraction toward some universal barycenter. Furthermore, the existence of some non-luminous, "dark" matter in galaxies could feasibly be within galaxy clusters too (specifically in the space between individual galaxies). By calculating the virial mass of each galaxy cluster, and comparing it to the summation of the virial masses of each of the cluster's galaxies, the total to 'luminous' mass ratios were found (luminous in the sense of inferred mass of visible galaxies). It was found that the virial mass of a cluster was generally hundreds of times larger than that of its luminous mass, with some clusters showing many thousands of times more dark mass. Figure 22 shows this distribution, with the mean total-to-luminous mass ratio being approximately $M_V/M_L = 637$. Just as this dark matter binds stars within a galaxy, larger (spatially) and more massive distributions of dark matter could be responsible for binding galaxies to a galaxy cluster.

As for whether these mass distributions are uniformly distributed throughout the universe, the homogeneity of the universe must be discussed and with it, the cosmological principle. Looking specifically at galaxies (as opposed to galaxy clusters), it was found that increasing distance from New Earth correlated with fewer observed galaxies. The hypothesized observational bias was discussed briefly in the Results section, but it is likely that there is, in fact, equal numbers of galaxies in equal volumes of space, with the smaller, dimmer galaxies not being observed from current-generation technology. Of course, the data obtained is unable to confirm this and so any claims of homogeneity in the universe cannot be currently validated. As such, with current data and technology, the universe *appears* not to be homogeneous.

The second aspect of the cosmological principle, isotropy, does appear to be upheld in the universe. Figure 20 shows that in approximately equal *absolute* areas of the sky, there is a uniform distribution of galaxy cluster counts. Figure 20a specifically shows no significant under or overdensities in the number density of galaxy clusters and so, on average, any position in the sky should show a roughly equal number of clusters.
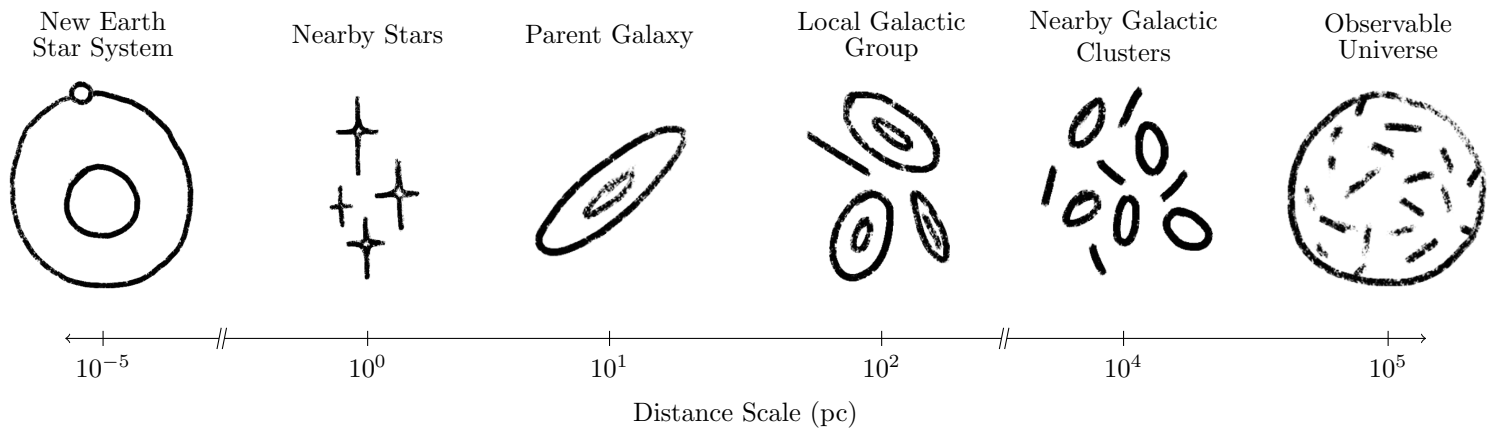
Figure. 24 Astronomical Distance Ladder

4   Conclusions

From the data recently obtained by the PPP and much analysis in Python, multiple revolutionary properties were calculated and inferred about the universe in which we live. Stars in the local neighbourhood were subject to blackbody model fits to their spectra with varying (but usually very good) accuracy. The temperatures of each of these stars was found by the shape of the blackbody spectrum, and it was found that the vast majority of stars are between 3000 and 10000K in temperature. By cross-analysing this distribution against produced colour-magnitude diagrams of local-stars, it was concluded that the vast majority of stars are dim, low-mass stars tending towards a red colouration.

By mapping the closest stars to New Earth, our home star system was found to belong to a disk galaxy for which we're approximately 50 ± 5 parsec distant from the center. The closest stars to New Earth were found to be on the roughly 5 to 20pc distant, and our galaxy was found to be part of an extremely local group which itself is part of a cluster of at least 52 galaxies. These cluster galaxies were found to be anywhere from 150pc away (for the very closest separate galaxies), up to 4300pc in distance, with most falling between 500 and 2000pc away from New Earth.

By studying radial velocity data of nearby stars, it was found that the majority of the stars in the universe belong to disk-shaped star clusters (galaxies) with coherent velocity profiles across their radii. On studying these velocity profiles, the existence of some non-luminous mass distribution within and around these galaxies were required to explain the logarithmic shape of the velocity curves seen. Large (and distant) galaxy clusters were also observed, with distances on the order of 10^5 pc, for which presence of this "dark" matter was also suggested via analysis of cluster dynamics with re-spect to the virial mass of each galaxy within the cluster.

A distance ladder of astronomical objects throughout the currently observable universe was devised, and shown in Figure 24.

Galaxies in the far universe were found to unanimously be moving towards New Earth on account of their spectral blueshift. This blueshift was larger for galaxies at larger distance. In fact, the radial velocity with respect to distance followed a linear trend extremely well, with an $R^2 = 0.994$ and a Hubble constant of $(-2.63 \pm 0.03) \times 10^3$ km.s^{-1}.Mpc. The Hubble time, or rather the approximate time until the "big crunch" of the universe was consequently 372 ± 5 million years from the date of observation.

The observable universe as a whole was found to be isotropic from the perspective of New Earth's position within the cosmos. Likely due to observational bias, however, the data indicates that the universe is *not* homogeneous. Over large distances, it was found that the number count of galaxies per equal-volume concentric shell decreased, although it is of the opinion of the writer that dimmer, lower mass galaxies were not detected at such distance and so were not included in the data set, ultimately leading to the conclusion of heterogeneity. Considering all of this, the theorized *cosmological principle* does not apply to our universe.

Observed phenomena for which our obtained data could not explain was suggested as topics for future research. This includes, but is not limited to: research of the three closest galaxies in the sky for which a dataset of stars could not isolated against the background "noise" of more optically compact galaxies, research into observing distant galaxies in other wavelengths (ideally in the infrared spectrum), and probes into the nature of dark matter.

References

[1] Malkin,   Z,   2019.   "A   New   Equal-Area   Isolatitudinal   Grid   on   a   Spherical   Surface",
https://arxiv.org/pdf/1909.04701.pdf

5   Appendices

5.1   Collaborator Contributions

Leo Clarke defined the period-luminosity relations for the variable stars, with some assistance from Ciaran Komarakul-Greene.

Ciaran contributed the colour-magnitude diagrams, and assisted with miscellaneous python programming and model derivations of which much of the analysis was built on.

Ryan White performed the bulk of the data analysis, including but not limited to: star coordinate transformation, star/galaxy map figures, star temperature analysis, identification of star clusters (galaxies) and galaxy clusters, matching X-ray sources to galaxy clusters and the resulting distance analysis, galaxy rotation curves, nearby galaxy parameter relations, and isotropy/homogeneity determination.

A very special thank you to Rika Matsubara-Park (@spacetato on instagram) for the drawings within Figure 24.

The complete set of data, programs in which it was analysed, and all produced figures are available at https://github.com/ryanwhite1/Distance_Ladder, along with a record of contributions by the group's members. If for any reason the link doesn't work, I'm available for contact via email: ryan.white@uqconnect.edu.au

5.2   Example Star Blackbody Fits

(a) Star P00015
Temperature $T = 15786 \pm 300$K

(b) Star P00024
Temperature $T = 8282 \pm 300$K

(c) Star P00104
Temperature $T = 4177 \pm 300$K

(d) Star P00157
Temperature $T = 76764 \pm 300$K

(e) Star P00254
Temperature $T = 5679 \pm 300$K

(f) Star P00276
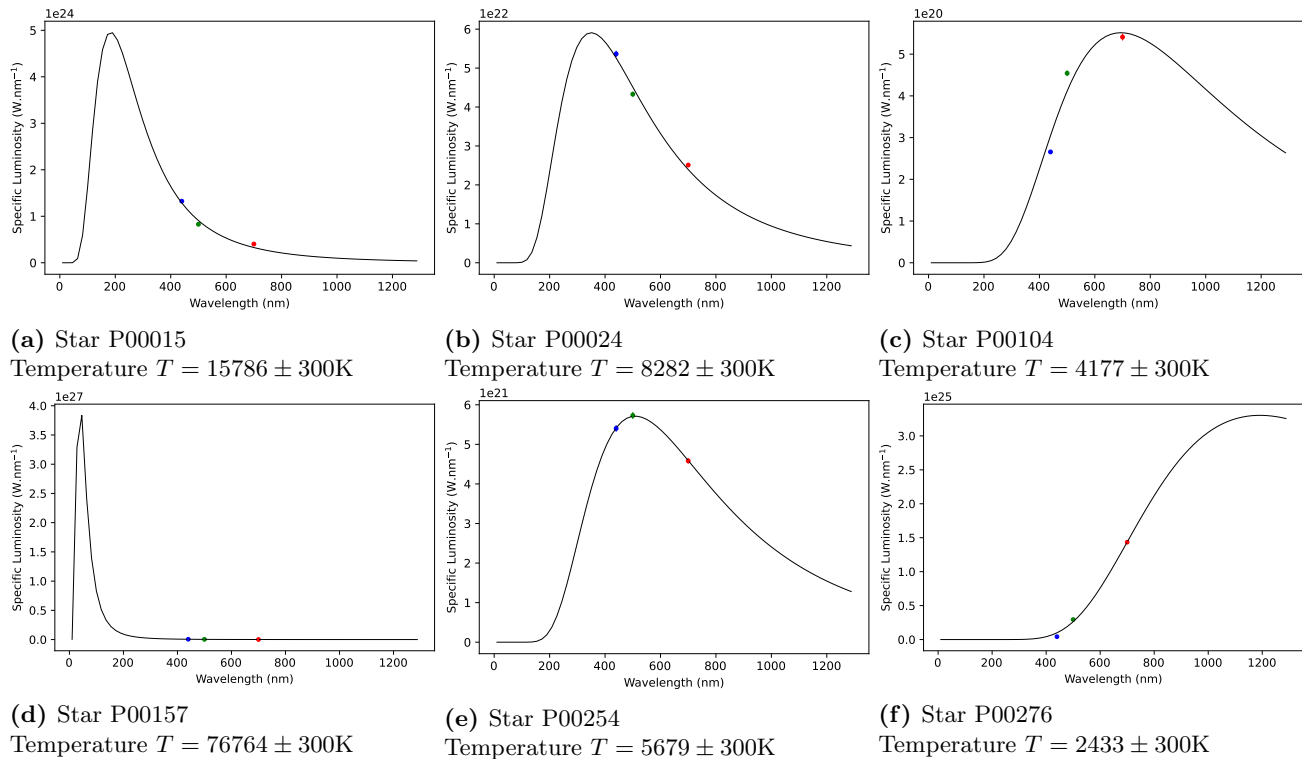Temperature $T = 2433 \pm 300$K

Figure. 25   Selected Fits of Blackbody Curves to Stellar Spectra Data
While some `curve_fit` outputs gave temperatures with uncertainties larger than 300K, only those with uncertainties below this threshold value were counted in the analysis. Some of the above fits have uncertainties *considerably* less than this 300K value, but it was rounded up for consistency and for a general baseline value. Errorbars in the Specific Luminosity values are present, although they are too small to be resolved at this scale of figure.

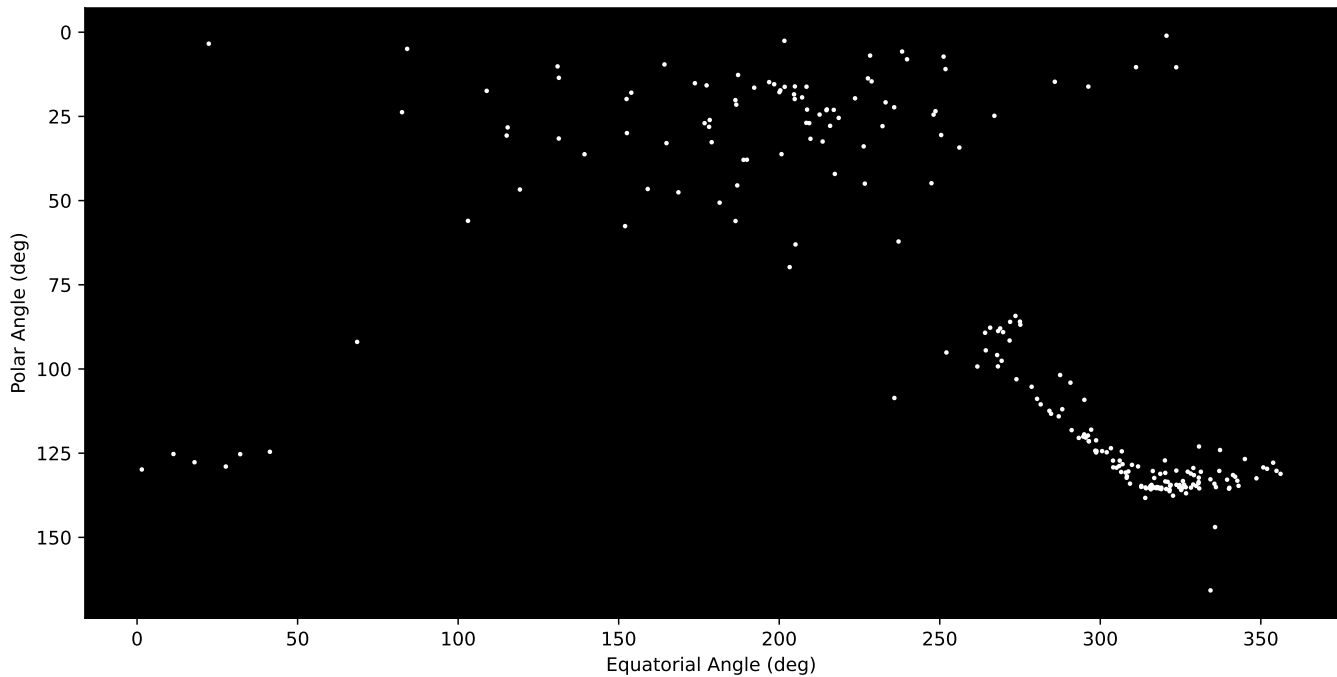## 5.3 All-Sky Map of Nearby Galaxies

Figure. 26 All-Sky Rectangular Projection of Nearby Galaxies
This figure uses an even more strict parallax threshold than Figure 23 ($p \geq 0.012$ vs $p > 0.007$ respectively). As such, it serves as an analogue to the 3D image, but focused on closer stars. The galaxy in which New Earth resides is shown in the bottom right of the figure, with the 'L' shape a result of the polar warping inherent with rectangular projections of spheres. The brightness and colour of stars do not represent any observable, and this plot shows purely the positions of close stars in the sky.

5.4 Geometry of New Earth with Respect to the Galactic Center
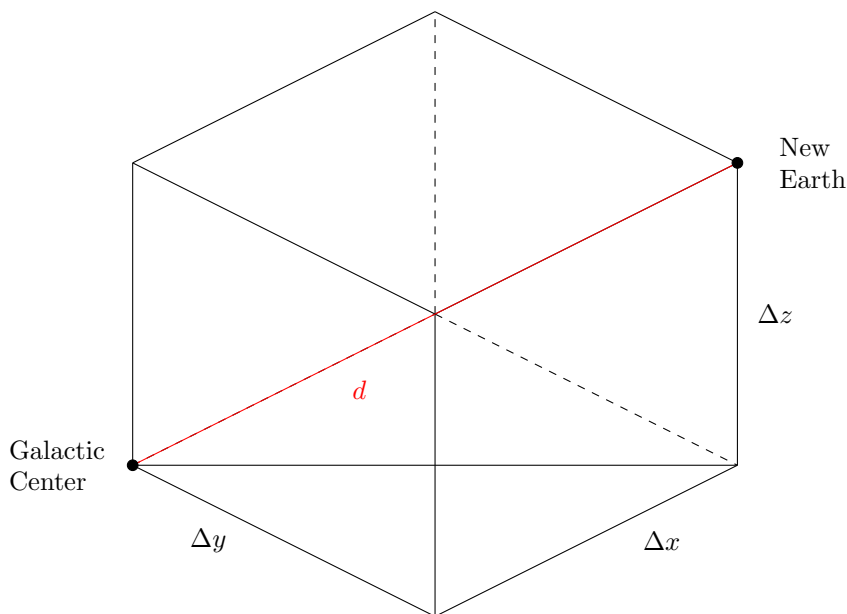
From the Jupyter interactive graph, each of the three measure-able distances are $\Delta x = 25 \pm 5$ pc, $\Delta y = -25 \pm 5$ pc, and $\Delta z = -35 \pm 5$ pc. Using a series of pythagoras equations, the distance that New Earth is from the Galactic Center is then

$$d = \sqrt{\left(\sqrt{25^2 + (-25)^2}\right)^2 + (-35)^2}$$
$$= \sqrt{25^2 + (-25)^2 + (-35)^2}$$
$$\simeq 50 \pm 5 \text{ pc}$$

Figure. 27 Geometric Picture of the New-Earth → Galactic Center Calculation
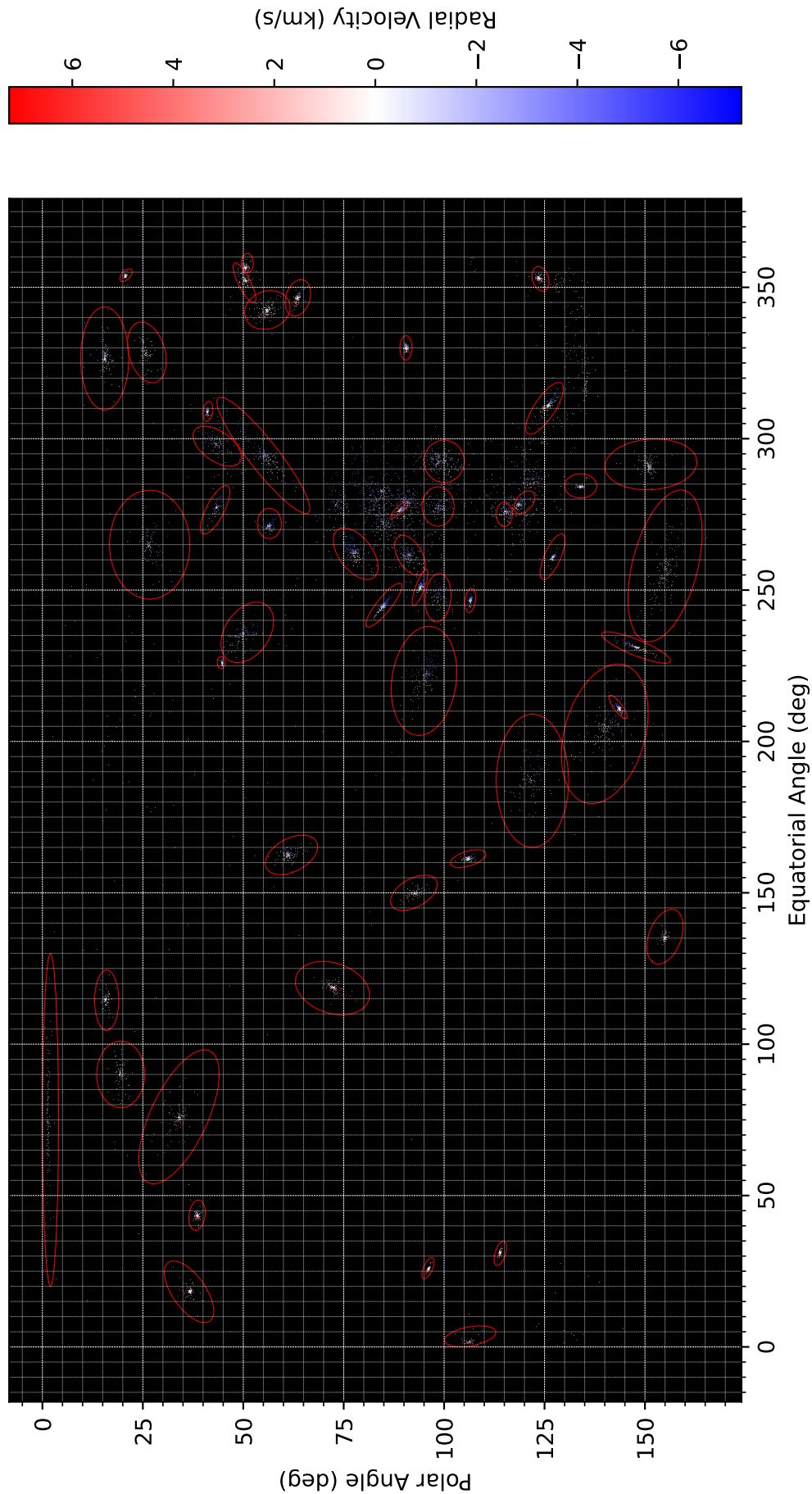
5.5   Redshift

Figure. 28 Analysis Image for Redshift of Stars

This image truly benefits from zooming in. Each ellipse defines a galaxy for which stars were then populated according to their position within the ellipse. Worth noting is that the extreme ellipticity of warped galaxy close to the poles did not affect analysis and is a visual artefact only.